ADVANCED FUNCTIONAL MATERIALS
www.afm-journal.de

3D Highly Stretchable Liquid Metal/Elastomer Composites with Strain-Enhanced Conductivity

Ruyue Fang, Bin Yao, Tianwu Chen, Xinwei Xu, Dingchuan Xue, Wei Hong, Hong Wang, Qing Wang,* and Sulin Zhang**

Current stretchable conductors, often composed of elastomeric composites infused with rigid conductive fillers, suffer from limited stretchability and durability, and declined conductivity with stretching. These limitations hinder their potential applications as essential components such as interconnects, sensors, and actuators in stretchable electronics and soft machines. In this context, an innovative elastomeric composite that incorporates a 3D network of liquid metal (LM), offering exceptional stretchability, durability, and conductivity, is introduced. The mechanics model elucidates how the interconnected 3DLM architecture imparts softness and stretchability to the composites, allowing them to withstand tensile strains of up to 500% without rupture. The relatively low surface-to-volume ratio of the 3DLM network limits the reforming of the oxide layer during cyclic stretch, thereby contributing to low permanent strain and enhanced durability. Additionally, the 3D architecture facilitates crack blunting and stress delocalization, elevating fracture resistance, while simultaneously establishing continuous conductive pathways that result in high conductivity. Notably, the conductivity of the 3DLM composite increases with strain during substantial stretching, highlighting its strain-enhanced conductivity. In comparison to other LM-based composites featuring 0D LM droplets, the 3DLM composite stands out with superior properties.

1. Introduction

The rise of wearable electronics and their applications in biomedical devices and soft robotics have promoted significant interests in the development of stretchable and durable conductors.[1] Traditional electronic devices predominantly utilize rigid materials, while biological tissues exhibit softness, high stretchability, and resilience.[2] To enhance softness and stretchability, current conductors utilize low-dimensional rigid materials with wavy configurations, such as metallic nanowires,[3] nanofilms,[4] carbon nanotubes,[5] and graphene sheets.[6] However, these conductors still fall short in matching the inherent softness and stretchability of natural tissues. Efforts to enhance toughness through rigid particle-filled polymers have shown promise by introducing additional energy dissipation mechanisms at the crack front.[7] Nonetheless, these composites still lack the fracture resilience observed in natural materials like animal skins, which exploit

---

R. Fang, T. Chen, D. Xue, S. Zhang
Department of Engineering Science and Mechanics
The Pennsylvania State University
University Park, PA 16802, USA
E-mail: suz10@psu.edu

B. Yao, Q. Wang, S. Zhang
Department of Materials Science and Engineering
The Pennsylvania State University
University Park, PA 16802, USA
E-mail: quw10@psu.edu

The ORCID identification number(s) for the author(s) of this article can be found under https://doi.org/10.1002/adfm.202310225

DOI: 10.1002/adfm.202310225

X. Xu, H. Wang
Department of Materials Science and Engineering
Shenzhen Engineering Research Center for Novel Electronic Information Materials and Devices & Guangdong Provincial Key Laboratory of Functional Oxide Materials and Devices
Southern University of Science and Technology
Shenzhen, Guangdong 518055, China
E-mail: wangh6@sustech.edu.cn

W. Hong
Department of Mechanics and Aerospace Engineering
Southern University of Science and Technology
Shenzhen, Guangdong 518055, China

S. Zhang
Department of Biomechanical Engineering
The Pennsylvania State University
University Park, PA 16802, USA

intricate multiscale and multimodal energy dissipation mechanisms.[8] Unfortunately, the inclusion of rigid fillers markedly increases stiffness, thereby compromising composites' softness. Recent strides have concentrated on developing soft and tough hydrogels with interpenetrating polymer double networks.[9] In these hydrogels, one network acts as a toughening agent by dissipating energy upon stretching, while the other maintains structural integrity and stretchability.[10] However, these double-network hydrogels exhibit significantly lower volumetric conductivity than metals. This challenge becomes even more significant when stretchable conductors need to maintain high conductivity under substantial stretching in their operating environments. Consequently, the task of creating highly stretchable conductors that seamlessly align with the properties of natural tissues for wearable electronics remains an unmet challenge.

In this study, we introduce a class of composite conductors that exhibit exceptional softness, high stretchability, and elevated durability by incorporating liquid metals (LMs) into an elastomeric matrix. In contrast to prior LM composites with 0D LM microdroplets,[2a,11] our composite leverages a 3D interconnected LM architecture. In conjunction with experimental characterizations, we establish a mechanics model to elucidate the outstanding softness, stretchability, high fracture resistance, and stretch-enhanced electrical conductivity of the 3DLM composite. Our combined experimental and modeling results not only offer insights for enhanced electro-mechanical properties of the LM composites but also unlock a wide array of applications in wearable electronics and soft robotics.

2. Results and Discussion

2.1. A Mechanics Model for LM-Elastomer Composites

Mechanical stretch generates a displacement field $\boldsymbol{u}$ over the material domain Ω_0. Considering the material heterogeneity, we divide the entire material domain into three subdomains $\Omega_0 = \Omega_{\mathrm{em}} + \Omega_{\mathrm{lm}} + \Omega_{\mathrm{ox}}$, where Ω_{em}, Ω_{lm}, and Ω_{ox} represent regions occupied by the elastomer, the liquid metal, and the oxide layer, respectively. The total strain energy of the composite encompasses these subdomains, as

$$\mathcal{F}_M\ (\mathbf{u}) = \int_{\Omega_{\mathrm{em}}} U_{\mathrm{em}}\,(\mathbf{u})\,d\Omega\ + \int_{\Omega_{\mathrm{lm}}} U_{\mathrm{lm}}\,(\mathbf{u})\,d\Omega + \int_{\Omega_{\mathrm{ox}}} U_{\mathrm{ox}}\,(\mathbf{u})\,d\Omega \tag{1}$$

where U_{em}, U_{lm}, and U_{ox} represent the respective strain energy densities within the subdomains.

To elucidate the deformation behavior of the composites, we assume incompressibility and negligible shear modulus for the LM conclusions. Under this assumption, the LM inclusions store negligible strain energy, $U_{\mathrm{lm}} = 0$. For the elastomer matrix, we employ a mixed Yeoh model[12] and Odgen–Roxburgh model to describe its hyper-elasticity and damage evolution. Within the Yeoh model, the strain energy density is decomposed into the deviatoric $U_{\mathrm{em}}^{\mathrm{dev}} = \sum_{i=1}^{3} C_{i0}(I_1 I_3^{-1/3} - 3)^{i}$ and volumetric components $U_{\mathrm{em}}^{\mathrm{vol}} = \sum_{i=1}^{3} D_{i0}(I_3^{1/2} - 1)^{2i}$, where C_{i0} and D_{i0} are material constants, and I_1 and I_3 are the respective first and third invariants of the strain tensor (values of the material constants are given in Supporting Information).

The Mullins effect, characterized by stress-softening due to microscale damage,[13] is incorporated through the Odgen-Roxburgh model. Here, a damage variable η is introduced to the strain energy function during unloading and subsequent submaximal reloading,[14] as

$$\eta\ =\ 1 - \frac{1}{\gamma}\mathrm{erf}\left[\frac{\hat{U}_{\mathrm{em}}^{\mathrm{dev}} - U_{\mathrm{em}}^{\mathrm{dev}}}{\alpha + \beta\,\hat{U}_{\mathrm{em}}^{\mathrm{dev}}}\right] \tag{2}$$

where α, β, and γ are material constants, and $\hat{U}_{\mathrm{em}}^{\mathrm{dev}}$ is the maximum value of $U_{\mathrm{em}}^{\mathrm{dev}}$ at a material point over its deformation history. Consequently, the strain energy density of the elastomer matrix can be written as

$$U_{\mathrm{em}} =\ \eta\,U_{\mathrm{em}}^{\mathrm{dev}} + U_{\mathrm{em}}^{\mathrm{vol}} + \psi\,(\eta) \tag{3}$$

Here $\psi(\eta)$ is a continuous damage function, defined as

$$\psi\,(\eta) = \int_{1}^{\eta} \left[\left(\alpha + \beta\,\hat{U}_{\mathrm{em}}^{\mathrm{dev}}\right)\mathrm{erf}^{-1}\,(\gamma\,(1-\eta))\right] d\eta\ + (1-\eta)\,\hat{U}_{\mathrm{em}}^{\mathrm{dev}} \tag{4}$$

and erf^{-1} is the inverse error function.

The oxide layer is inherently brittle and undergoes repeated breaking and reforming during stretching and releasing of the composite, introducing extrinsic plasticity into the LM inclusions. To model this, we treat the oxide layer as an elasto-plastic material, featuring both elastic and plastic components in its strain energy density function, as

$$U_{\mathrm{ox}} = \frac{\lambda}{2}\left(\mathrm{tr}\varepsilon_{\mathrm{e}}\right)^2 + \mu\,\mathrm{tr}\left(\varepsilon_{\mathrm{e}}^2\right) + \sigma_{\mathrm{y}}\varepsilon_{\mathrm{ep}} \tag{5}$$

where the first two terms represent the elastic strain energy density in terms of elastic strain $\boldsymbol{\varepsilon}_{\mathrm{e}}$, with λ and μ being the two Lame constants. Neglecting the strain-hardening effect, the plastic dissipation is constructed by the yield strength σ_{y} and the equivalent plastic strain $\varepsilon_{\mathrm{ep}}$. Without considering the detailed breaking-reforming process, we set a vanishing Poisson's ratio for the oxide layer to mimic its spontaneous growth during stretching. To account for energy dissipation through plastic yielding during unloading, we estimate the yield strength by equating the plastic work to the work done by friction between the sliding oxide layers.

We enforce mechanical equilibrium in the entire domain, as

$$\frac{\delta\mathcal{F}_M}{\delta\mathbf{u}}\ =\ \nabla.\sigma\ =\ 0 \tag{6}$$

where $\boldsymbol{\sigma}$ is the Cauchy stress. Under prescribed displacement boundary conditions, the equilibrium equation is solved to obtain the stress-strain relationships and the stress distribution within the composites.

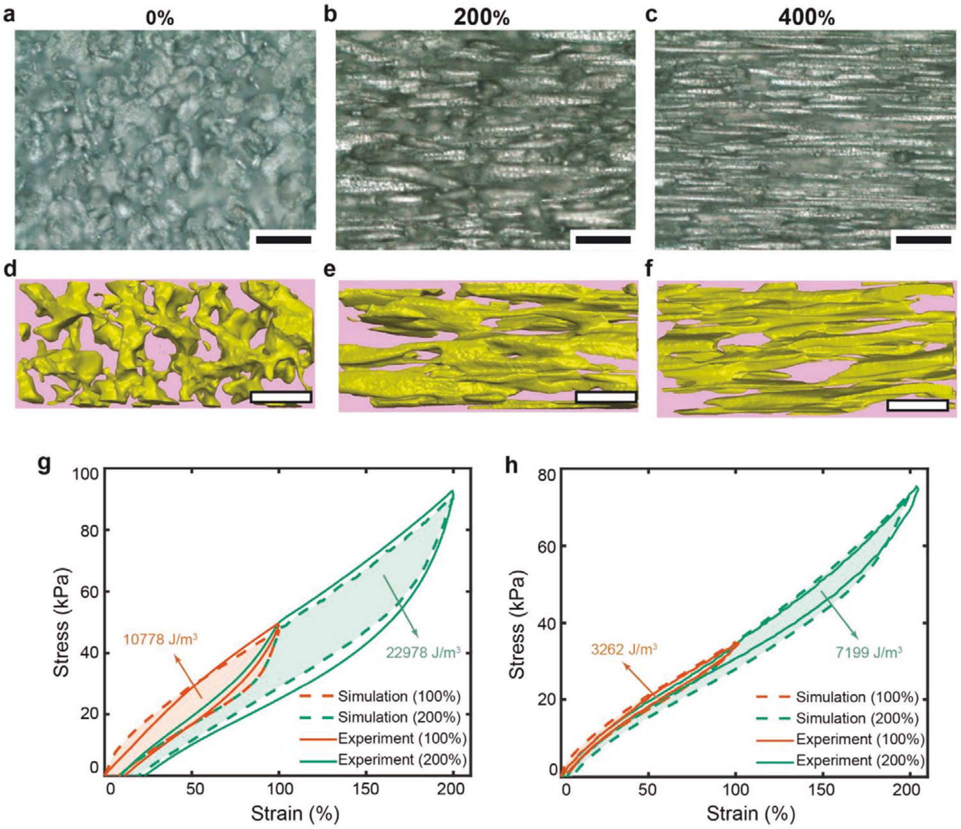

Figure 1. Tensile test results of the LM-elastomer composites. a–c) Optical images of the 0DLM composites under 0%, 200%, and 400% strains, respectively. Scale bars: 50 µm. d,e) Micro-CT images of the 3DLM composites under 0%, 200%, and 400% strains, respectively. Scale bars: 500 µm. g,h) Stress–strain curves of the 0DLM (g) and 3DLM (h) composites under cyclic loading. Solid and dashed red lines represent the first loading and unloading by experiments and simulations, respectively, and solid and dashed blue lines denote the second loading and unloading curves.

2.2. High Stretchability, Low Modulus, and Low Permanent Strain of the LM-Elastomer Composites

In our experiments, both 0D LM droplets and 3D interconnected LM inclusions made of the eutectic gallium-indium alloy (EGaIn, 75% Ga and 25% In, by weight) were embedded into an elastomeric matrix (Ecoflex 00–30, Smooth-On) to formulate the LM composites (**Figure 1**a,d and Supporting Information). Despite sharing an equal volume fraction of LM content (30%), these two types of composites exhibited distinct structural arrangements. The 0DLM droplets, with ~16 µm in diameter, were juxtaposed against the 3D LM skeleton, which was ~100 µm in thickness. Our comprehensive measurements unveiled the exceptional mechanical attributes of the LM composites, characterized by low modulus, high stretchability, and low permanent strain following cyclic loading. When subject to stretching, the LM inclusions elongated and rotated along the stretch directions (Figure 1a–f). Impressively, both the LM composites showcased the ability to ensure tensile strains of up to 500% without rupture (Figure S1, Supporting Information). The rupture strains aligned with that of the unfilled, pure elastomer, indicating that the presence of LM inclusions does not compromise the stretchability of the elastomer matrix. Intriguingly, our numerical results from the mechanics model replicated the stress–strain curves of the experiments under cyclic loading, thereby affirming the model's capacity in capturing the primary deformation and energy-dissipation mechanisms inherent to these composites (Figure 1g,h). During the stretching process, the Young's modulus of the LM composites exhibited an initial decrease followed by a pronounced increase, yielding a S-shaped stress–strain curve as anticipated by the Yeoh model. This nonlinear behavior is likely attributed to the gradual alignment of polymer chains within the elastomer matrix during stretch. Cyclic loading introduced the Mullin's effect, delineating hysteresis. Notably, the 0DLM composite displayed a greater hysteresis than the 3DLM composite (Figure 1g,h), signifying more efficient energy dissipation mechanisms during stretching in the former. Impressively, even after enduring 10 000 stretching and releasing cycles at 250% strain over 1 s per cycle, no cracks nor deterioration in electrical conductivity were observed, demonstrating the mechanical robustness and stability of the 3DLM composites (Figure S2, Supporting Information).

Our measurements indicated that the Young's modulus of the unfilled pure elastomer used in our experiments ranged from 70 to 90 kPa (**Figure 2**a). In comparison, the moduli of the LM composites ranged from 30 to 70 kPa, implying a softening effect due to the presence of the LM inclusions. Remarkably, these composites even surpassed the softness of human skin (~100 kPa)[15] and further reduction in moduli could be achieved by utilizing elastomers with lower moduli. Correspondingly, the Young's moduli of all three composites exhibited an initial decline followed by

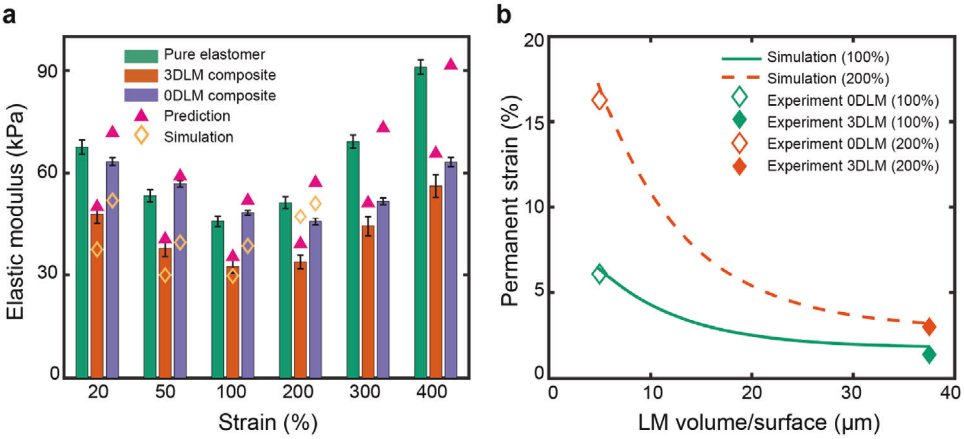

Figure 2. a) Elastic moduli of the unfilled pure elastomer and the LM composites under various strained states. b) Permanent strain at different volume/surface ratio of LM inclusions corresponding to different stretched states.

an increase with applied stretching, with the 3DLM composite consistently exhibiting the lowest modulus across all the stretching states. Our modeling results, shown by the open diamonds in Figure 2a, closely aligned with the general trend observed in experimental measurements, although minor disparities existed.

Apart from direct numerical modeling, the reduced modulus of the composites can be elucidated by Eshelby's theory. [16] This theory posits that the composite's Young's modulus, denoted by E_c, can be approximated by $E_c = E/(1 + 5\varphi/3)$, with E being the Young's modulus of the elastomer matrix and φ representing the volume fraction of the LM inclusions. While Eshelby's theory serves as a foundation, it predicts the same Young's modulus for the 0DLM and 3DLM composites for the same φ, which is inconsistent with our experimental characterizations. This discrepancy arises from the omission of surface tension of the microscopic inclusions, particularly when the inclusion length scale falls below the elastocapillary length $L \equiv \gamma_0/E$.[17] This length scale accounts for effective surface tension γ_0 of the LM inclusions, considering the presence of the oxide layer. To extend Eshelby's theory to microscale inclusions, Dufrense et al. predicted the Young's modulus of composites, factoring in the surface tension effect,[18] as

$$E_c = E\frac{1+\frac{5}{2}\frac{L}{R}}{\frac{5}{2}\frac{L}{R}(1-\varphi)+\left(1+\frac{5}{3}\varphi\right)} \tag{7}$$

This expression is reduced to Eshelby's theory when the radius of the inclusions $R \gg L$. The equivalent surface tension of the oxide layer is 0.624 N m^{-1}[11e,19] and the Young's modulus of the elastomer matrix is ~70 kPa, yielding an elastocapillary length of L ~9 µm. For the 0DLM composite, the radius (~8 µm) is comparable to the elastocapillary length, while the characteristic length of the 3DLM composite (50 µm) is much larger. The predicted moduli at various strains by the extended Eshelby's theory are denoted as filled triangles in Figure 2a. The size and surface tension effects of the LM inclusions explain why the 3DLM composite is softer than its 0D counterpart.

Our measurements revealed that the 3DLM composite also incurred less permanent strain compared to the 0DLM composite when undergoing the same amount of stretch (Figure 2b). With the elastomer bearing minimal inelastic strain, the permanent strain of the composite predominantly stemmed from the LM inclusions. Given the identical volume fraction of LM inclusions in both LM composites, variations in the oxide layer's surface area emerged as the primary factor influencing the permanent strain. Assuming both the LM inclusions and the elastomer matrix are incompressible, stretching changes the shape of the LM inclusions, leading to an increase of the surface area of the LM inclusions, approximately by $A_\lambda = A_0\sqrt{\lambda}$, where $\lambda = 1 + \varepsilon$ is the stretch, and ε is the strain. Microscopically, this permanent strain is closely entwined with the breaking and reforming of the oxide layer. During stretching, the surface area of the oxide layer trends to expand. Given its fragility and propensity to self-healing due to GaIn's high reactivity with oxide residues within the polymer, the oxide layer undergoes repeated breaking and reforming. During unloading, the LM inclusions tend to reduce their surface area. Consequently, the newly formed oxide layer undergoes breakage, resulting in friction upon overlap with other oxide layers. This friction translates into energy dissipation, contributing to the permanent strain. This theoretical analysis was substantiated by simulations at various stretching states (hence the volume to surface ratio of the LM inclusions varies), as shown in Figure 2b, revealing that an increased volume/surface ratio of LM inclusions may mitigate permanent strain. Another evidence is in Figure 1g,h where the 0DLM composites have larger energy dissipation than its 3D counterpart.

2.3. Fracture Mechanisms

We assessed the fracture energy of both the unfilled elastomer and the LM composites using the pure shear tear method introduced by Rivlin and Thomas.[10b,20] In these tests, a notched sample was subjected to stretching until rupture occurred at a critical distance d_c. Then, an un-notched sample with matching dimensions was stretched to rupture at a critical distance d_f ($d_f > d_c$). The work of fracture $W(d_f)$ of the un-notched sample was determined as the area beneath the load-stretch curve. The material's fracture energy, denoted by Γ, corresponds to the energy required to stretch the un-notched sample to the same critical stretch,

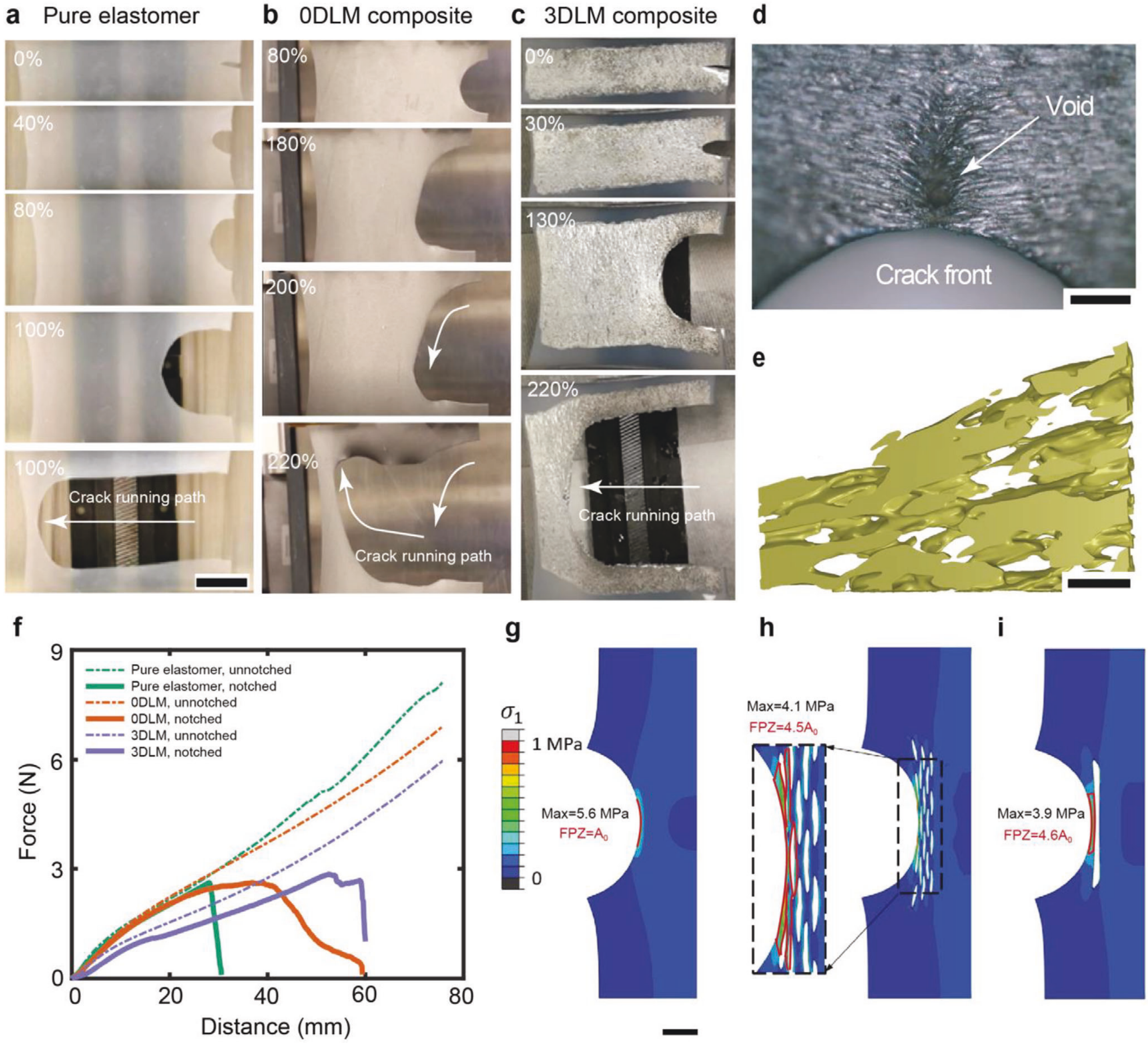

Figure 3. Pure shear tear tests of notched samples of a) pure elastomer, b) 0DLM composite. and c) 3DLM composite, showing crack-tip blunting and crack running paths. Scale bar: 20 mm. All the specimens are in the mm scale. The LM inclusions at the crack tips align with the principal stress (tensile) direction. The crack of 0DLM composite takes a turn during propagation, while the crack running path of 3DLM composite is in the same direction. d) Optical image of the crack-tip morphology of the 0DLM composite, showing the elongation and alignment of the LM droplets as well as the emergence of a void in front of the crack tip. Scale bar: 100 µm. e) 3D reconstructed structures by Micro-CT around the crack tip of the 3DLM composite at 180% strain, showing the alignment of the LM skeleton along the direction of the first-principal stress. Scale bar: 500 µm. f) Fracture tests for pure elastomer and the two LM composites, with the same sample dimensions and the same initial notch size. g–i) Stress concentration around the crack tip in pure elastomer (g), 0DLM (h), and 3DLM (i) composites. The contours marked by red lines denote the fracture process zone (FPA) in each case. Scale bar: 2 mm.

calculated by $\Gamma = W(d_c)/A$, with A being the cross-sectional area of the sample in its undeformed state (~70 mm^2). The onset and propagation of the crack, as well as the morphological changes of the LM inclusions at the crack front, were examined using micro-computed microtomography (micro-CT) and optical microscopy (**Figure 3**a–c).

For the unfilled elastomer samples, tensile loading caused notch blunting. As stretching continued, the blunted notch expanded horizontally until complete rupture occurred. For the 3DLM composite, notch blunting was more pronounced, extending over nearly the entire transverse direction of the sample. However, notch propagated at a significantly slower pace, indicative of its higher fracture resistance compared to the unfilled elastomer samples. The 0DLM composite exhibited notch blunting on an intermediate level between the unfilled elastomer and the 3DLM composite. Differently, crack propagation in the 0DLM composite was frequently diverted. Fracture energies of 758 J m^{-2} were measured for the unfilled elastomer, 2440 J m^{-2} for the 0DLM composite, and 1863 J m^{-2} for the 3DLM composite. Evidently, the LM inclusions substantially enhanced the fracture toughness of the elastomer matrix, with the dispersed 0DLM droplets yielding a stronger toughening effect than the 3DLM network.

To appreciate the toughening mechanisms of the LM inclusions, we constructed a 2D plain-stress model to assess the stress field, deformation pattern, and crack propagation paths at the notch front. Our model utilized pre-notched samples with identical notch length a_0. Circular LM droplets situated at the notch front simulated the 0DLM composite, whereas a single rectangular LM inclusion represented the 3DLM composite (Figure 3h,i). The volume fraction of the LM inclusions was kept the same across the simulation samples and oxide layers were introduced onto the surface of LM inclusions. Tensile load was applied to initiate and propagate the notches. Our simulations revealed delocalized stress distribution, large-scale energy dissipation, and both crack blunting and deflection in the presence of LM inclusions, which contribute to the toughening effect of the LM composites.

Given their inherent softness, LM inclusions could deform readily into different shapes in response to the crack-tip stress field, thereby enabling stress redistribution and delocalization. Our simulation results demonstrated that under equivalent stretching, the unfilled elastomer displayed the highest first-principal stress at the crack tip, while the 3DLM composite exhibited the lowest stress levels (Figure 3h,i). The presence of LM inclusions yielded stress discontinuity across the LM-elastomer-interface. The ligament bridges of the elastomer matrix between the LM inclusions transmitted high-level stress to regions further from the crack tip in the 0DLM composite. High-level stress regions also spread out at the crack tip of the 3DLM composite. In contrast, the stress was more localized in the unfilled elastomer and the 3DLM composite. This stress delocalization corresponds to a more uniform deformation behavior, preventing localized failure and enhancing the toughness of the composites.

In soft materials, only a small fraction of the released energy contributes to the fracture process, specifically the breaking of polymer chains.[21] Most of the energy is instead mechanically dissipated in regions around the crack.[22] This mechanical dissipation frequently appears as hysteresis loops in the stress-strain curves of the material, a result of plasticity and partial damage.[23] As shown in Figure 1g,h, the 0DLM composite demonstrates a superior mechanical dissipation capacity compared to the 3DLM composite. Analogous to the flexible molecular chains in the polymeric network of a rubber, the flexible nature of the elastomeric ligament facilitated nearly complete dissipation of stored elastic energy upon rupture at the crack tip.[24] This "elastic dissipater" mechanism, commonly employed in the development of flaw-insensitive composites,[25] was evident in the LM composites, although the presence of LM inclusions introduced additional energy dissipation mechanisms. Under mechanical stress, the LM inclusions elongated and rotated to align with the direction of the local first principal stress (Figure 3d,e). These shape changes enabled the LM inclusions to permanently dissipate some applied mechanical energy. Simultaneously, the elongation triggered breaking, reforming, and sliding of the oxide layer, further contributing to energy dissipation. These energy dissipation mechanisms collectively mitigated stress concentration at the crack tip, impeding crack propagation and enhancing overall toughness. The flexible deformation of LM inclusions enlarged the energy dissipation regions at the crack tip, commonly referred to as the process zone. The enlarged process zone indicates that the crack tip is shielded from the mechanical loading, indicating more mechanical dissipation and therefore enhanced toughness.[22] Calculations based on damage significance in relation to the maximal stress (above 5% of the maximal stress) suggested that the process zone size at crack tips was the largest for the 0DLM composite and smallest for the unfilled elastomer samples.

Upon encountering a LM inclusion, a crack could be diverted and forced to circumvent or infiltrate the LM inclusion. The LM inclusions may also act as a crack arrestor by blunting the crack. This dual mechanism of crack blunting and deflection enhanced the fracture resistance of the composite. Owing to the relatively low LM concentration, complete tear elimination[11e] did not occur in our LM composites. Consequently, the failure strain of notched LM composites was notably lower than the un-notched counterparts. Furthermore, our simulations indicated that cracks tended to propagate into the LM droplets in the 0DLM composites (Figure S3, Supporting Information), leading to complete rupture of the LM droplets and deflecting the fracture path. This crack deflection was more pronounced due to the random spatial distribution of LM droplets in the 0DLM composite, resulting in frequent crack deflection during the fracture process, as observed in our tests (Figure 3b). For the 3DLM composite, our simulations revealed that both crack propagation into and diversion from the LM inclusions were energetically feasible (Figure S3, Supporting Information). Given the 3D interconnected architecture of the LM inclusions in the 3DLM composite, rupture of the LM network could not cause crack deflection, but only blunting. This additional crack deflection toughening explained the higher fracture energy for 0DLM composite than the 3DLM composite.

2.4. The Enhanced Electrical Conductivity

To characterize the interplay between mechanical stretching and electrical properties, we conducted measurements of the electrical conductivity of the composites at various stretched states using a custom four-probe method. As the elastomer matrix is an insulator and the LM is a conductor, the electrical conductivity of the LM-elastomer composites is contingent upon the connectivity of the LM inclusions within the composites. Indeed, we found that under the stress-free conditions, with the same LM volume fraction (30%), the electrical conductivity of 3DLM composites surpasses that of the 0DLM composite by 14–17 orders of magnitude (**Figure 4**a,b). The substantial discrepancy can be attributed to the presence of continuous, 3D conductive pathways in the 3DLM composites, in contrast to the fragmented paths stemming from isolated LM droplets in the 0DLM composite.

We performed simulations to determine the effective conductivity at various stretched states. At each stretched state dictated by the mechanics model, we selected a unit cell of the composites and applied a voltage V across it to generate current (Figure 4c,d).

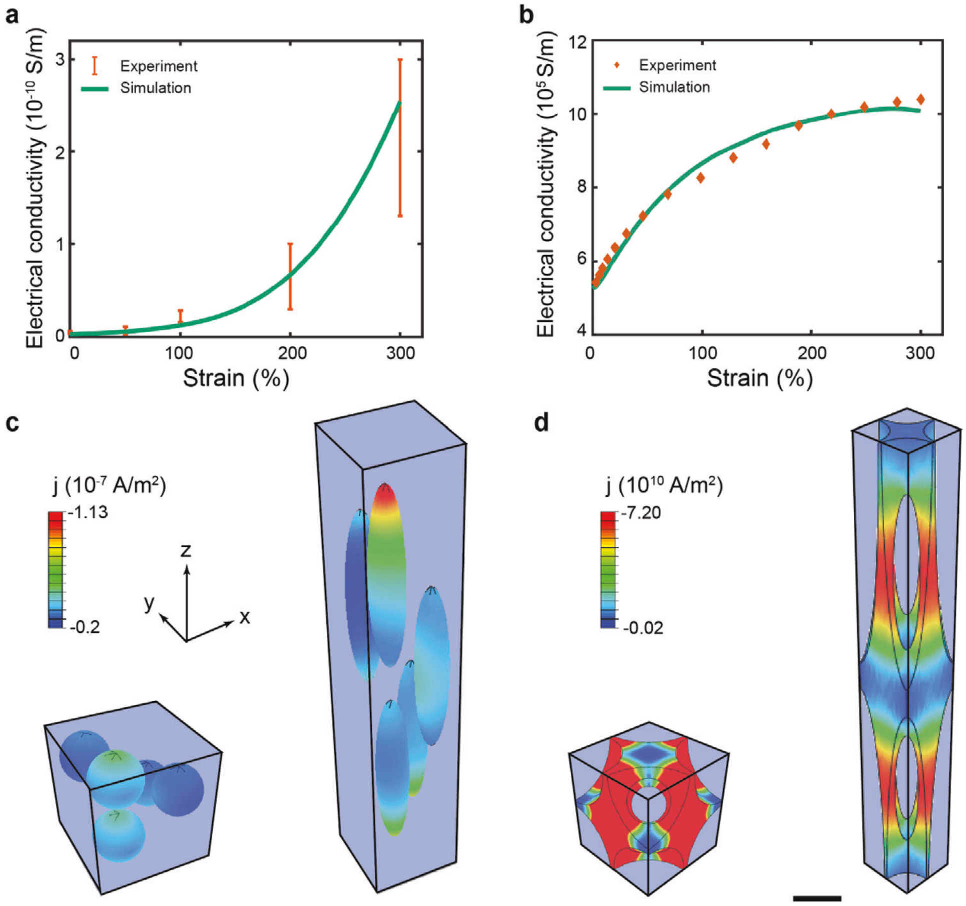

Figure 4. a,b) Electrical conductivities of the 0DLM (a) and 3DLM (b) composites as a function of stretch. c,d) Model predictions of the electrical current density at stress-free (left) and 200% strain for the 0DLM (d) and 3DLM (e) composites. The sample is initially a cube of side length 100 µm and the applied voltage is 1 V. Scale bar: 50 µm.

We solved the Poisson's equation to acquire the electrical potential distribution and current density. Given the substantial contrast in electrical conductivity between the elastomer matrix and LM inclusions, the current density exhibited significant spatial variation. The effective electrical conductivity of the composites was estimated by $\bar{\omega} = \frac{LJ}{AV}$, with J being the total current across the cross-section area A, and L representing the length of the unit cell. Our simulation results on the effective conductivity of the composites demonstrated an excellent alignment with the experimental measurements (Figure 4a,b). Upon inspecting the contours of electrical current density (Figure 4c,d), a noteworthy observation is that the elastomer matrix does not conduct any electrical current. This phenomenon can be attributed to the robust connectivity of the conductive paths within the 3DLM composite. Conversely, the 0DLM composite essentially functions as electrical insulators, owing to the isolated nature of the LM droplets in the matrix, resulting in an extremely low electrical conductivity.

Remarkably, the electrical conductivity of both LM composites increases with mechanical stretching. When stretching to 400% strain, the conductivity of the 0DLM composite increases by near two orders of magnitude, albeit remaining at a low level. In contrast, the conductivity of the 3DLM composite exhibits a consistent rise with stretching, escalating from 5.3×10^5 S m^{-1} under stretch-free conditions to 1.0×10^6 S m^{-1} at 300% strain. This stretch-induced enhancement of conductivity in the LM composites diverges from the behavior observed in stretchable conductors employing rigid fillers such as metals,[26] carbon nanotubes,[27] and graphene layers.[4a,6a] The stretch-enhanced electrical conductivity can be attributed to the stretch-induced alignment and elongation of the LM inclusions. As previously illustrated, when the composites undergo stretching, the LM inclusions tend to elongate and align themselves along the stretching direction, which may densify the conductive paths, leading to enhanced electrical conductivity.

3. Conclusions

In summary, our experimental characterizations show that the 3DLM composite exhibits a lower Young's modulus, reduced permanent strain, and much higher electrical conductivity compared to the 0DLM composite. Our mechanics analysis reveals that the differences arise from the volume fraction of the oxide layer. According to the extended Eshelby's theory, surface tension effect impacts the modulus, which accounts for the lower Young's modulus of the 3DLM composite. The repeated breaking and reforming of the oxide layer account for the inelastic deformation of the LM composites. The relatively lower volume fraction of the oxide layer in the 3DLM composite explains the lower permanent strain under cyclic stretch. Furthermore, the remarkable toughness of the LM composites can be attributed to the crack-tip blunting, stress delocalization, and adaptive shape changes of the LM inclusions. In the 0DLM composite, cracking path deflection presents an additional energy dissipation mechanism, pointing to the reason of its higher fracture energy than the 3DLM composites.

Notably, the 3DLM composite is highly conductive, with a conductivity surpassing that of the 0DLM composite by many orders of magnitude. Unlike other stretchable conductors, whose conductivity typically degrades under stretching,[3a,28] the 3DLM composite exhibits enhanced conductivity along the stretch direction. This superior performance, alongside with its high stretchability and durability, opens an extensive array of applications in wearable electronics and soft robotics.

Supporting Information

Supporting Information is available from the Wiley Online Library or from the author.

Acknowledgements

R.F. and B.Y. contributed equally to this work. Q.W. and S.Z. acknowledge the supports of the National Science Foundation (CMMI 1933398 and ECCS 2035051).

Conflict of Interest

The authors declare no conflict of interest.

Data Availability Statement

The data that support the findings of this study are available from the corresponding author upon reasonable request.

Keywords

fracture, liquid–metal composites, stretchable electronics

Received: August 26, 2023
Revised: October 3, 2023
Published online:

---

[1] a) T. Someya, Z. Bao, G. G. Malliaras, *Nature* **2016**, *540*, 379; b) M. L. Hammock, A. Chortos, B. C. Tee, J. B. Tok, Z. Bao, *Adv. Mater.* **2013**, *25*, 5997; c) S. Lee, S. Shin, S. Lee, J. Seo, J. Lee, S. Son, H. J. Cho, H. Algadi, S. Al-Sayari, D. E. Kim, T. Lee, *Adv. Funct. Mater.* **2015**, *25*, 3114; d) B. Zhang, J. Lei, D. Qi, Z. Liu, Y. Wang, G. Xiao, J. Wu, W. Zhang, F. Huo, X. Chen, *Adv. Funct. Mater.* **2018**, *28*, 1801683; e) J. Lee, B. Llerena Zambrano, J. Woo, K. Yoon, T. Lee, *Adv. Mater.* **2020**, *32*, 1902532; f) J. Chen, Q. Peng, T. Thundat, H. Zeng, *Chem. Mater.* **2019**, *31*, 4553; g) Y. Cui, S. N. Kim, S. E. Jones, L. L. Wissler, R. R. Naik, M. C. Mcalpine, *Nano Lett.* **2010**, *10*, 4559; h) J. A. Rogers, T. Someya, Y. Huang, *Science* **2010**, *327*, 1603; i) Y. Gao, X. Jiang, P. Wang, Y. Zhong, T. Lu, *Extreme Mech. Lett.* **2023**, *61*, 102016; j) S. Lin, H. Yuk, T. Zhang, G. A. Parada, H. Koo, C. Yu, X. Zhao, *Adv. Mater.* **2016**, *28*, 4497; k) Q. Zhang, X. Chen, B. Zhang, T. Zhang, W. Lu, Z. Chen, Z. Liu, S. H. Kim, B. Donovan, R. J. Warzoha, E. D. Gomez, J. Bernholc, Q. M. Zhang, *Matter* **2021**, *4*, 2448.

[2] a) E. J. Markvicka, M. D. Bartlett, X. Huang, C. Majidi, *Nat. Mater.* **2018**, *17*, 618; b) S. Wang, Y. Nie, H. Zhu, Y. Xu, S. Cao, J. Zhang, Y. Li, J. Wang, X. Ning, D. Kong, *Sci. Adv. 8*, eabl5511.

[3] a) S. Choi, S. I. Han, D. Jung, H. J. Hwang, C. Lim, S. Bae, O. K. Park, C. M. Tschabrunn, M. Lee, S. Y. Bae, J. W. Yu, J. H. Ryu, S.-W. Lee, K. Park, P. M. Kang, W. B. Lee, R. Nezafat, T. Hyeon, D.-H. Kim, *Nat. Nanotechnol.* **2018**, 1048; b) D. Son, J. Kang, O. Vardoulis, Y. Kim, N. Matsuhisa, J. Y. Oh, J. W. To, J. Mun, T. Katsumata, Y. Liu, A. F. Mcguire, M. Krason, F. Molina-Lopez, J. Ham, U. Kraft, Y. Lee, Y. Yun, J. B.-H. Tok, Z. Bao, *Nat. Nanotechnol.* **2018**, 1057; c) C. Cho, W. Shin, M. Kim, J. Bang, P. Won, S. Hong, S. H. Ko, *Small* **2022**, *18*, 2202841; d) P. Lee, J. Lee, H. Lee, J. Yeo, S. Hong, K. H. Nam, D. Lee, S. S. Lee, S. H. Ko, *Adv. Mater.* **2012**, *24*, 3326.

[4] a) Y. Wang, C. Zhu, R. Pfattner, H. Yan, L. Jin, S. Chen, F. Molina-Lopez, F. Lissel, J. Liu, N. I. Rabiah, Z. Chen, J. W. Chung, C. Linder, M. F. Toney, B. Murmann, Z. Bao, *Sci. Adv.* **2017**, *3*, e1602076; b) Y.-S. Guan, A. Thukral, S. Zhang, K. Sim, X. Wang, Y. Zhang, F. Ershad, Z. Rao, F. Pan, P. Wang, J. Xiao, C. Yu, *Sci. Adv. 6*, eabb3656.

[5] a) T. Sekitani, Y. Noguchi, K. Hata, T. Fukushima, T. Aida, T. Someya, *Science* **2008**, *321*, 1468; b) D. J. Lipomi, M. Vosgueritchian, B. C. Tee, S. L. Hellstrom, J. A. Lee, C. H. Fox, Z. Bao, *Nat. Nanotechnol.* **2011**, *6*, 788; c) F. Xu, X. Wang, Y. Zhu, Y. Zhu, *Adv. Funct. Mater.* **2012**, *22*, 1279.

[6] a) N. Liu, A. Chortos, T. Lei, L. Jin, T. R. Kim, W. G. Bae, C. Zhu, S. Wang, R. Pfattner, X. Chen, R. Sinclair, Z. Bao, *Sci. Adv.* **2017**, *3*, e1700159; b) Z. Wang, X. Liu, X. Shen, N. M. Han, Y. Wu, Q. Zheng, J. Jia, N. Wang, J.-K. Kim, *Adv. Funct. Mater.* **2018**, *28*, 1707043; c) S. J. Kim, K. Choi, B. Lee, Y. Kim, B. H. Hong, *Annu. Rev. Mater. Res.* **2015**, *45*, 63.

[7] a) J.-Z. Liang, *J. Appl. Polym. Sci.* **2002**, *83*, 1547; b) J. K. Kim, R. E. Robertson, *J. Mater. Sci.* **1992**, *27*, 161; c) A. C. Balazs, T. Emrick, T. P. Russell, *Science* **2006**, *314*, 1107; d) S.-C. Wong, A. Baji, A. N. Gent, *Compos. Part A Appl. Sci. Manuf.* **2008**, *39*, 579.

[8] W. Yang, V. R. Sherman, B. Gludovatz, E. Schaible, P. Stewart, R. O. Ritchie, M. A. Meyers, *Nat. Commun.* **2015**, *6*, 6649.

[9] a) S.-H. Shin, W. Lee, S.-M. Kim, M. Lee, J. M. Koo, S. Y. Hwang, D. X. Oh, J. Park, *J. Chem. Eng.* **2019**, *371*, 452; b) L. Hu, P. L. Chee, S. Sugiarto, Y. Yu, C. Shi, R. Yan, Z. Yao, X. Shi, J. Zhi, D. Kai, H. D. Yu, W. Huang, *Adv. Mater.* **2023**, *35*, 2205326; c) H. Zhu, X. Hu, B. Liu, Z. Chen, S. Qu, *ACS Appl. Mater. Interfaces* **2021**, *13*, 59243; d) G. Shi, X. Peng, J. Zeng, L. Zhong, Y. Sun, W. Yang, Y. L. Zhong, Y. Zhu, R. Zou, S. Admassie, Z. Liu, C. Liu, E. I. Iwuoha, J. Lu, *Adv. Mater.* **2023**, *35*, 2300109.

[10] a) J. P. Gong, Y. Katsuyama, T. Kurokawa, Y. Osada, *Adv. Mater.* **2003**, *15*, 1155; b) J.-Y. Sun, X. Zhao, W. R. K. Illeperuma, O. Chaudhuri, K. H. Oh, D. J. Mooney, J. J. Vlassak, Z. Suo, *Nature* **2012**, *489*, 133.

[11] a) B. Yao, W. Hong, T. Chen, Z. Han, X. Xu, R. Hu, J. Hao, C. Li, H. Li, S. E. Perini, M. T. Lanagan, S. Zhang, Q. Wang, H. Wang, *Adv. Mater.* **2020**, *32*, 1907499; b) M. D. Bartlett, A. Fassler, N. Kazem, E. J. Markvicka, P. Mandal, C. Majidi, *Adv. Mater.* **2016**, *28*, 3726; c) L. Li, Y. Mao, L. Zhao, L. Li, J. Wu, M. Zhao, W. Du, L. Yu, P. Jiang, *Nat. Commun.* **2019**, E10; d) C. Pan, E. J. Markvicka, M. H. Malakooti, J. Yan, L. Hu, K. Matyjaszewski, C. Majidi, *Adv. Mater.* **2019**, *31*, 1900663; e) N. Kazem, M. D. Bartlett, C. Majidi, *Adv. Mater.* **2018**, *30*, 1706594.

[12] O. H. Yeoh, *Rubber Chem. Technol.* **1993**, *66*, 754.

[13] J. Diani, B. Fayolle, P. Gilormini, *Eur. Polym. J.* **2009**, *45*, 601.

[14] R. W. Ogden, D. G. Roxburgh, *Proc. R. Soc. A: Math. Phys. Eng.* **1999**, *455*, 2861.
[15] C. Pailler-Mattei, S. Bec, H. Zahouani, *Med. Eng. Phys.* **2008**, *30*, 599.
[16] J. D. Eshelby, *Proc. R. Soc Lond. A Math. Phys. Sci.* **1957**, *241*, 376.
[17] a) X. Shi, Z. Liu, L. Feng, T. Zhao, C.-Y. Hui, S. Zhang, *Phys. Rev. X* **2022**, 12; b) R. W. Style, C. Hyland, R. Boltyanskiy, J. S. Wettlaufer, E. R. Dufresne, *Nat. Commun.* **2013**, 4.
[18] R. W. Style, R. Boltyanskiy, B. Allen, K. E. Jensen, H. P. Foote, J. S. Wettlaufer, E. R. Dufresne, *Nat. Phys.* **2015**, *11*, 82.
[19] a) D. Wang, X. Wang, W. Rao, *Acc. Mater. Res.* **2021**, *2*, 1093; b) M. D. Dickey, R. C. Chiechi, R. J. Larsen, E. A. Weiss, D. A. Weitz, G. M. Whitesides, *Adv. Funct. Mater.* **2008**, *18*, 1097.
[20] R. S. Rivlin, A. G. Thomas, *J. Polym. Sci.* **1953**, *10*, 291.
[21] R. Long, C.-Y. Hui, *Soft Matter* **2016**, *12*, 8069.
[22] X. Zhao, *Soft Matter* **2014**, *10*, 672.
[23] T. Zhang, S. Lin, H. Yuk, X. Zhao, *Extreme Mech. Lett.* **2015**, *4*, 1.
[24] a) Z. Ma, X. Feng, W. Hong, *J. Appl. Mech.* **2015**, 83; b) G. J. Lake, A. G. Thomas, *Proc. R. Soc Lond. A Math. Phys. Sci.* **1967**, *300*, 108.
[25] C. Chen, Z. Wang, Z. Suo, *Extreme Mech. Lett.* **2017**, *10*, 50.
[26] a) M. Park, J. Im, M. Shin, Y. Min, J. Park, H. Cho, S. Park, M.-B. Shim, S. Jeon, D.-Y. Chung, J. Bae, J. Park, U. Jeong, K. Kim, *Nat. Nanotechnol.* **2012**, *7*, 803; b) N. Matsuhisa, D. Inoue, P. Zalar, H. Jin, Y. Matsuba, A. Itoh, T. Yokota, D. Hashizume, T. Someya, *Nat. Mater.* **2017**, *16*, 834.
[27] a) K.-Y. Chun, Y. Oh, J. Rho, J.-H. Ahn, Y.-J. Kim, H. R. Choi, S. Baik, *Nat. Nanotechnol.* **2010**, *5*, 853; b) F. Schütt, S. Signetti, H. Krüger, S. Röder, D. Smazna, S. Kaps, S. N. Gorb, Y. K. Mishra, N. M. Pugno, R. Adelung, *Nat. Commun.* **2017**, *8*, 1215.
[28] a) F. Xu, Y. Zhu, *Adv. Mater.* **2012**, *24*, 5117; b) Y. Kim, J. Zhu, B. Yeom, M. Di Prima, X. Su, J.-G. Kim, S. J. Yoo, C. Uher, N. A. Kotov, *Nature* **2013**, *500*, 59.